UNIVERSITY OF BIRMINGHAM
University of Birmingham Research at Birmingham

Principles of nanoparticle imaging using surface plasmons

Demetriadou, Angela; Kornyshev, Alexei A

DOI:
10.1088/1367-2630/17/1/013041

License:
Creative Commons: Attribution (CC BY)

Document Version
Publisher's PDF, also known as Version of record

Citation for published version (Harvard):
Demetriadou, A & Kornyshev, AA 2015, 'Principles of nanoparticle imaging using surface plasmons', *New Journal of Physics*, vol. 17, 013041. https://doi.org/10.1088/1367-2630/17/1/013041

Link to publication on Research at Birmingham portal

General rights
Unless a licence is specified above, all rights (including copyright and moral rights) in this document are retained by the authors and/or the copyright holders. The express permission of the copyright holder must be obtained for any use of this material other than for purposes permitted by law.

•Users may freely distribute the URL that is used to identify this publication.
•Users may download and/or print one copy of the publication from the University of Birmingham research portal for the purpose of private study or non-commercial research.
•User may use extracts from the document in line with the concept of 'fair dealing' under the Copyright, Designs and Patents Act 1988 (?)
•Users may not further distribute the material nor use it for the purposes of commercial gain.

Where a licence is displayed above, please note the terms and conditions of the licence govern your use of this document.

When citing, please reference the published version.

Take down policy
While the University of Birmingham exercises care and attention in making items available there are rare occasions when an item has been uploaded in error or has been deemed to be commercially or otherwise sensitive.

If you believe that this is the case for this document, please contact UBIRA@lists.bham.ac.uk providing details and we will remove access to the work immediately and investigate.

Download date: 08. May. 2024

New Journal of Physics
The open access journal at the forefront of physics

Deutsche Physikalische Gesellschaft DPG IOP Institute of Physics

PAPER • OPEN ACCESS

Principles of nanoparticle imaging using surface plasmons

To cite this article: Angela Demetriadou and Alexei A Kornyshev 2015 *New J. Phys.* **17** 013041

View the article online for updates and enhancements.

Related content

- Surface plasmon polaritons: physics and applications
  Junxi Zhang, Lide Zhang and Wei Xu
- Near-field photonics: surface plasmon polaritons and localized surfaceplasmons
  Anatoly V Zayats and Igor I Smolyaninov
- Radiation guiding with surface plasmon polaritons
  Zhanghua Han and Sergey I Bozhevolnyi

Recent citations

- Complex Resonant Scattering Behavior in the Surface Plasmon Resonance Imaging Microscopy of Single Gold Nanorods
  Yunshan Fan *et al*
- Determining the Aggregation Kinetics of Nanoparticles by Single Nanoparticle Counting
  Di Jiang *et al*
- Tracking Interfacial Dynamics of Single Nanoparticle Using Plasmonic Scattering Interferometry
  Haibo Chen *et al*

This content was downloaded from IP address 147.188.75.175 on 22/03/2021 at 13:45

New Journal of Physics
The open access journal at the forefront of physics

Deutsche Physikalische Gesellschaft DPG
IOP Institute of Physics

Published in partnership with: Deutsche Physikalische Gesellschaft and the Institute of Physics

OPEN ACCESS

RECEIVED
11 October 2014

ACCEPTED FOR PUBLICATION
21 November 2014

PUBLISHED
20 January 2015

Content from this work may be used under the terms of the Creative Commons Attribution 3.0 licence.

Any further distribution of this work must maintain attribution to the author (s) and the title of the work, journal citation and DOI.

PAPER

Principles of nanoparticle imaging using surface plasmons

Angela Demetriadou and Alexei A Kornyshev

Department of Chemistry, Imperial College London, Prince Consort Road, SW7 2AZ, London, UK

E-mail: a.demetriadou06@imperial.ac.uk

Keywords: surface plasmon microscopy, surface plasmon diffraction, plasmonic image, single particle spectroscopy, nanoparticles, surface plasmon polaritons

Abstract

Unlike surface plasmon resonance sensors that detect integral changes to the optical properties of a sample, surface plasmon polariton-microscopy techniques can detect isolated nanoparticles in real-time through their plasmonic image, even of sub-wavelength dimensions. The feature characteristics and intensity of this plasmonic image are dependent on the nanoparticle's chemical composition and size. However, the lack of a theoretical model describing the principles forming a plasmonic image have hindered their understanding. In this article, we present a full-wave analytical model that describes electromagnetically the formation of the plasmonic image. Through our analytical model and numerical calculations, we show the properties of a plasmonic image from sub-wavelength to macroscopic particles of various chemical compositions.

1. Introduction

Surface plasmon polaritons (SPPs) are bound electromagnetic waves, which are evanescently excited and propagate on metal–dielectric interfaces. SPPs are ideal for sensing purposes due to their environmental sensitivity and their significantly enhanced and spatially confined fields at a metal–dielectric interface. Due to the very narrow-band resonance exciting SPPs, SPP-based sensors are used mainly to measure integral changes arising from bio-molecular interactions [1–3], binding properties of analytes [4], changes to physical quantities [5, 6], chemical sensing of analyte concentrations [7–10], biosensing of protein–protein interactions [11], detection of biological and chemical analytes [12, 13], environmental monitoring [14], food safety [15] and medical diagnostics [16]. However, it is very difficult with existing SPP-sensor methodologies to detect the presence of nanoparticles in very dilute solutions, since their integral signal is not strong enough.

Evanescent waves have also being utilized for microscopy techniques, such as total internal reflection fluorescence (TIRF) microscopy, where in combination with fluorescence emission image mainly biological samples of μm-scale. The resolution of TIRF microscopy can be potentially improved to sub-100 nm by taking advantage of the nonlinear fluorophore response. But this requires long acquisition times and therefore the procedure suffers from photo-bleaching and photo-toxicity. Recently though, Zybin *et al* [17] proposed a label-free SPP microscopy technique that images in real-time single isolated nanoparticle of just few tens of nanometers in diameter. This technique, unlike TIRF microscopy, is label-free and non-perturbative, and therefore has advantages over standard probe methods, such as Scanning Tunnelling Microscope and Atomic Force Microscope. Since then, SPP-microscopy have been utilized for imaging and detection of sub-wavelength particles, such as single DNA molecules [18, 19] and viruses [20]. Despite the promising applications of SPP microscopy, currently there is no correlation between the properties of a plasmonic image (i.e. an image formed due to an object's interaction with a SPP-wave) with the geometrical and material features of a particle.

In this paper, we present a full-wave theoretical model describing the physics behind SPP-microscopy for both sub-wavelength and macroscopic particles. The plasmonic images observed with SPP-microscopy are due to the diffraction of the SPP waves by a single isolated nanoparticle, which are diverted into three distinct channels [21, 22]. We show through our analytical model that not all the diffraction channels contribute to the plasmonic images observed with SPP-microscopy. Since this analytical model is applicable from sub-wavelength to macroscopic nanoparticles, it goes beyond the electrostatic approach of dipolar approximation, which is

© 2015 IOP Publishing Ltd and Deutsche Physikalische Gesellschaft

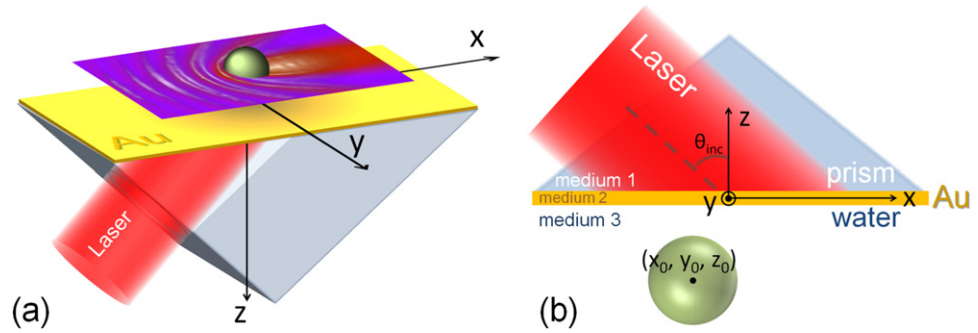

Figure 1. The Kretschmann configuration, where a laser is incident on a thin metal film through the prism, exciting a surface plasmon polariton (SPP). (a) An illustration of the SPP diffraction by a nanoparticle. (b) The axes configuration with respect to the Kretschmann set-up. The nanoparticle is positioned with its centre at (x_0, y_0, z_0). (figures not in scale)

limited to nanoparticles much smaller than the wavelength of light [23, 24], the implementation of Green's functions [22] which require a semi-analytical solution for particles away from the quasi-static limit and the use of effective boundary conditions [25] requiring a full-numerical solution of integral equation [26–28]. Hence, our findings can lead to the spectroscopic characterization of an isolated nanoparticle, further invigorating the capabilities of SPP-microscopy techniques. Finally, it is straightforward to extend our work for THz SPPs, which have been recently exploited for time-resolved imaging of μm-particles [29].

2. Diffraction of surface plasmon waves by a nanoparticle

When a single particle is placed in the path of a SPP-wave, then, as any wave would, the SPP is diffracted. However, in this case the SPP-wave is diffracted into three distinctive channels [22]. Furthermore, when the particle is in close proximity to the metal–dielectric interface, the optimum conditions for the evanescent coupling to a SPP-excitation change locally, since the refractive index of the particle differs from its environment's. Hence, the plasmonic image is created due to both the local changes of the optical properties, and the diffraction disturbances the particle induces to the SPP wave, which can be imaged in real-time. For SPP-microscopy, the plasmonic image is observed at a single angle from the surface normal, and is therefore carried to the far-field by the reflected beam from the metal slab.

In this work we consider the Kretschmann configuration (figure 1) for the excitation of SPP-waves, which is widely used to study adsorbates, as the platform for the theoretical interpretation of the plasmonic image observed experimentally. However, it should be emphasized that our work and theoretical model are applicable for any other configurations of SPP-excitation. The Kretschmann configuration consists of a prism with refractive index n_1 and a thin layer of metal with thickness d_m and refractive index n_2, deposited on one of the prism's sides. The metal slab is illuminated with a laser through the prism and a SPP-wave is excited in medium 3, which has a refractive index n_3 (figure 1). Note that the SPP can be coupled to only evanescently and is therefore excited when $n_3 < n_1$. The optimum condition for the SPP excitation exist at a single laser wavelength and for a fixed angle of incidence, and vice versa.

Consider an incident wave propagating through the prism and incident on the thin metal slab, with electromagnetic fields $\mathbf{H} = (H_x, H_y, H_z)$ and $\mathbf{E} = (E_x, E_y, E_z)$, guided by $\mathbf{k_0} = (k_x, k_y, k_z)$ (the system's axes are defined in figure 1). Only its TM mode (i.e. $H_z = 0$ component) can couple to an evanescent SPP [30] and it follows from Maxwell's equations that the generalized field equation describing a SPP wave in medium n_3 is given by:

$$\mathbf{E}_3 = \frac{B \exp\left(\left|k_{3z}\right| z\right)}{\omega \varepsilon_3 \varepsilon_0}\left[\mathrm{i}k_{3z}\hat{\mathbf{e}}_x + \mathrm{i}\left(\frac{k_{3z}k_y}{k_x}\right)\hat{\mathbf{e}}_y - \left(k_x + \frac{k_y^2}{k_x}\right)\hat{\mathbf{e}}_z\right] \exp\left(\mathrm{i}k_x x + \mathrm{i}k_y y\right), \quad (1)$$

where k_x, k_y and k_{3z} are the SPP wavevectors in medium n_3, given by $k_x = n_1|k_0| \sin\theta_{\mathrm{inc}} \cos\phi_{\mathrm{inc}}$, $k_y = n_1|k_0| \sin\theta_{\mathrm{inc}} \sin\phi_{\mathrm{inc}}$ and $k_{3z} = -n_3|k_0|\sqrt{1 - \left(n_1 \sin\theta_{\mathrm{inc}}/n_3\right)^2}$, where θ_{inc} and ϕ_{inc} are the laser's angles of incidence on the metal slab. B is a coefficient dependent on the materials of the SPP-sensor (i.e. prism and metal) and the incident wavevector k_0. Since throughout this paper the sensor and incident radiation are kept the same, B remains a constant. The first term of (1) gives the evanescent component of the SPP-wave that decays exponentially away from the metal–dielectric interface into medium 3. The second term of (1), which is in

square brackets, determines the vector direction of **E**, defined by the wavevector components of the incident laser. The last term describes the phase propagation of the SPP-wave along the metal–dielectric interface. Note that different excitation methods for the SPP would simply change the value of B and no other term of (1).

If we consider, for analytical simplicity, a spherically-shaped particle, then the incident SPP-wave given by (1) needs to be expressed in spherical harmonics (and is denoted as $\mathbf{E}_i$ for the rest of the manuscript). We expand the phase propagating part of (1) in generalized spherical harmonic polynomials using the Jacobi–Angler expansion, and transform the vector term of (1) into a spherical coordinate system (see supplementary information). Hence, the incident SPP E-field on a spherical particle is:

$$\mathbf{E}_i = \frac{B\exp\left(\left|k_{3z}\right| r\cos\theta\right)}{\omega\varepsilon_3\varepsilon_0}\mathbf{E}_0\sum_{n=0}^{\infty}\sum_{m=-n}^{m=n}4\pi \mathrm{i}^n j_n\left(k_{xy}r\right)Y_n^m(\theta,\phi)\overline{Y_n^m\left(\theta_k,\phi_k\right)}, \tag{2}$$

where j_n is the spherical Bessel function, $k_{xy}=\sqrt{k_x^2+k_y^2}$ is the phase propagating SPP wavevector, r, θ and ϕ are the spatial spherical coordinates with origin at a random point (x_0, y_0, z_0) [1]. θ_k and ϕ_k are the spherical components of k_{xy}, Y_n^m is the spherical harmonic function[2] and $\overline{Y_n^m}$ is its complex conjugate. $\mathbf{E}_0$ transformed to the spherical coordinate system is expressed as: $\mathbf{E}_0=\left[E_{0i}^r\hat{\mathbf{e}}_r+E_{0i}^\theta\hat{\mathbf{e}}_\theta+E_{0i}^\phi\hat{\mathbf{e}}_\phi\right]$.

A nanoparticle of radius r_p with its centre at (x_0, y_0, z_0), as shown in figure 1(b), and refractive index n_p, which can be dispersive, diffracts a SPP-wave into three different channels: (i) a SPP channel, where the scattered fields retain their SPP and evanescent nature and therefore are still bound on and propagate along the metal–dielectric interface, (ii) a radiative channel, where part of the incident SPP-wave decouples from the metal–dielectric interface and now propagates (or radiates) away from the particle in medium 3 [21, 22], and (iii) a finite slab (FS) channel, where the radiative component described above, interacts with the finite metal slab. Therefore, the diffracted E-fields in medium 3 from the interaction of a SPP-wave with a spherical particle are given by: $\mathbf{E}_s=\mathbf{E}_s^{\mathrm{SPP}}+\mathbf{E}_s^{\mathrm{rad}}+\mathbf{E}_s^{\mathrm{FS}}$. SPP-waves also decouple from the metal–dielectric interface at the presence of surface defects, which have been investigated in the past by Sanchez *et al* [31, 32] and Zayats *et al* [33].

Diffraction into the SPP-channel comes only from the tangential field components, since the boundary conditions enforce that the incident and scattered tangential fields to be continuous at the interface between the particle and its environment. Therefore the tangential components of the scattered E-field need to have an SPP-nature and are given by:

$$\mathbf{E}_s^{\mathrm{SPP}} = \frac{B\exp\left(\left|k_{3z}\right| r\cos\theta\right)}{\omega\varepsilon_3\varepsilon_0}\sum_{n=0}^{\infty}\sum_{m=-n}^{m=n}4\pi \mathrm{i}^n\left(a_{n\theta}E_{0i}^\theta\hat{\mathbf{e}}_\theta+a_{n\phi}E_{0i}^\phi\hat{\mathbf{e}}_\phi\right)h_n^{(1)}\left(k_{xy}r\right)Y_n^m(\theta,\phi)\overline{Y_n^m\left(\theta_k,\phi_k\right)}, \tag{3}$$

where $h_n^{(1)}$ is the spherical Hankel function of the first kind, and $a_{n\theta}$ and $a_{n\phi}$ are the scattering coefficients dependent on the particle's radius and refractive index and govern the vector direction of the scattered fields. On the other hand, the normal component of the E-field is diffracted into the radiative channel and given by:

$$\mathbf{E}_s^{\mathrm{rad}} = \frac{B\exp\left(\left|k_{3z}\right| r_p\cos\theta\right)}{\omega\varepsilon_3\varepsilon_0}\sum_{n=0}^{\infty}\sum_{m=-n}^{m=n}4\pi \mathrm{i}^n a_{nr}E_{0i}^r h_n^{(1)}\left(k_{xy}r\right)Y_n^m(\theta,\phi)\overline{Y_n^m\left(\theta_k^{\mathrm{rad}},\phi_k^{\mathrm{rad}}\right)}\hat{\mathbf{e}}_r, \tag{4}$$

where a_{nr} is the radiative scattering coefficient. The amplitude of the radiative component is not decaying exponentially away from the metal slab, since the wave has lost its evanescent properties, but is dependent only on the amplitude of the SPP-wave incident on the nanoparticle. Additionally, although the wavevector carrying the radiative fields has the same argument k_{xy} as the propagating component of the incident SPP-wave, now it also has a z-component expressed with the non-zero value of θ_k^{rad}.

Finally, only the radiative component can interact with the finite metal slab, by being reflected and even transmitted in it, unlike the SPP-scattered component, which is just bound on the metal–dielectric interface. Hence, the scattering from the finite slab (i.e. FS-channel) is a consequence of the radiative ($\mathbf{E}_s^{\mathrm{rad}}$) component's interaction with the metal slab. However, both the FS- and the radiative channels do not contribute to the plasmonic image of a particle observed with SPP-microscopy, since both channels emit a signal at all angles, while the plasmonic image is observed at a single θ away from the metal–prism interface. In fact for most dielectric nanoparticles (composed of realistic materials) the radiative component is not significant, rendering the FS-component negligibly small. Hence, we choose to neglect the FS-channel, since no information are lost for the plasmonic image and we avoid a cumbersome analytical representation.

[1] These can be defined as $r=\sqrt{(x-x_0)^2+(y-y_0)^2+(z-z_0)^2}$, $\theta=\cos^{-1}\left((z-z_0)/r\right)$ and $\phi=\tan^{-1}\left((y-y_0)/(x-x_0)\right)$.

[2] $Y_n^m(\theta,\phi)=\sqrt{\frac{(2n+1)(n-m)!}{4\pi(n+m)!}}P_n^m(\cos\theta)\mathrm{e}^{\mathrm{i}m\phi}$, where P_n^m is the associated Legendre Polynomial.

Contrary to the scattered fields, the fields inside the nanoparticle are transmitted in just two channels: the tangential components as (i) SPP-waves given by:

$$\mathbf{E}_l^{\mathrm{SPP}} = \frac{B\exp\left(N\left|k_{3z}\right|r\cos\theta\right)}{\omega n_p^2\varepsilon_0}\sum_{n=0}^{\infty}\sum_{m=-n}^{m=n}4\pi \mathrm{i}^n\left(b_{n\theta}E_{0i}^{\theta}\hat{\mathbf{e}}_{\theta}+b_{n\phi}E_{0i}^{\phi}\hat{\mathbf{e}}_{\phi}\right)j_n\left(Nk_{xy}r\right)Y_n^m(\theta,\phi)\overline{Y_n^m\left(\theta_k,\phi_k\right)} \tag{5}$$

and (ii) propagating or radiative waves given by:

$$\mathbf{E}_l^{\mathrm{rad}} = \frac{B\exp\left(N\left|k_{3z}\right|r_p\cos\theta\right)}{\omega n_p^2\varepsilon_0}\sum_{n=0}^{\infty}\sum_{m=-n}^{m=n}4\pi \mathrm{i}^n b_{nr}E_{0i}^{r}j_n\left(Nk_{xy}r\right)Y_n^m(\theta,\phi)\overline{Y_n^m\left(\theta_k^{\mathrm{rad}},\phi_k^{\mathrm{rad}}\right)}\hat{\mathbf{e}}_r, \tag{6}$$

where $N = n_p/n_3$ is the refractive index ratio between the nanoparticle and its surrounding medium and $b_{nr,\theta,\phi}$ are the internal coefficients, which govern the vector components of the internal fields.

The scattering ($a_{nr,\theta,\phi}$) and internal ($b_{nr,\theta,\phi}$) coefficients can be found by imposing the boundary conditions at the interface between the nanoparticle and its environment and are given by:

$$a_{nr} = -\frac{\mathrm{i}(N-1)}{N+1}\left(\frac{j_n(N\rho)\left[j_n(\rho)\right]' - Nj_n(\rho)\left[j_n(N\rho)\right]'}{Nh_n^{(1)}(\rho)\left[j_n(N\rho)\right]' - j_n(N\rho)\left[h_n^{(1)}(\rho)\right]'}\right), \tag{7}$$

$$a_{n\theta} = a_{n\phi} = \frac{j_n(N\rho)\left[j_n(\rho)\right]' - Nj_n(\rho)\left[j_n(N\rho)\right]'}{Nh_n^{(1)}(\rho)\left[j_n(N\rho)\right]' - j_n(N\rho)\left[h_n^{(1)}(\rho)\right]'}, \tag{8}$$

$$b_{nr} = \frac{\exp\left(\left|k_{3z}\right|r_p\cos\theta\right)j_n(\rho)}{\exp\left(N\left|k_{3z}\right|r_p\cos\theta\right)j_n(N\rho)} - \frac{\omega\varepsilon_0}{Im\left(n_p^2\right)n_p^2E_{0i}^{r}j_n(\rho)}, \tag{9}$$

$$b_{n\theta} = b_{n\phi} = \left(\frac{N^2\exp\left(\left|k_{3z}\right|r_p\cos\theta\right)}{\exp\left(N\left|k_{3z}\right|r_p\cos\theta\right)}\right)\left(\frac{h_n^{(1)}(\rho)\left[j_n(\rho)\right]' - j_n(\rho)\left[h_n^{(1)}(\rho)\right]'}{Nh_n^{(1)}(\rho)\left[j_n(N\rho)\right]' - j_n(N\rho)\left[h_n^{(1)}(\rho)\right]'}\right), \tag{10}$$

where $\rho = k_{xy}r_p$, $N = n_p/n_3$ and r_p is the radius of the nanoparticle. Note that due to the spherical symmetry of the nanoparticle $a_{n\theta} = a_{n\phi}$ and $b_{n\theta} = b_{n\phi}$. Here it should be noted that (5) and (6) slightly over-estimate the E-fields inside the nanoparticle, since they assume that the SPP-wave excited inside the nanoparticle has the same excitation coefficient B as in the environment surrounding it (i.e. medium 3). One can take into account the different excitation coefficient B' inside the nanoparticle, but then would also need to consider the SPP-wave excited in medium 3 and transmitted inside the nanoparticle with an amplitude proportional to B. This method though further complicates the derivation of the $a_{n,r\theta\phi}$ and $b_{n,r\theta\phi}$, and hence the analytical model, without providing any physical insight. In the section 3, we show that the internal fields do not significantly contribute to the plasmonic image of a nanoparticle (which is our final aim to obtain analytically), and therefore allows for the above assumption.

Finally, the diffracted fields caused by the SPP-interaction with any spherical object are given by the fields inside the particle ($\mathbf{E}_l$) and fields outside of the particle by the superposition of the scattered and incident fields ($\mathbf{E}_i + \mathbf{E}_s$):

$$\mathbf{E} = \begin{cases} \mathbf{E}_l^{\mathrm{SPP}} + \mathbf{E}_l^{\mathrm{rad}} & \text{for } r \leqslant r_p, \\ \mathbf{E}_i + \mathbf{E}_s^{\mathrm{SPP}} + \mathbf{E}_s^{\mathrm{rad}} + \mathbf{E}_s^{\mathrm{FS}} & \text{for } r > r_p \end{cases} \tag{11}$$

for inside and outside the particle respectively. The above model describes all the fields in medium 3, from which the plasmonic image emerges.

2.1. Analysis of diffracted fields

We apply the above analytical model for nanoparticles of various sizes and refractive indices in an aqueous solution (i.e. $n_3 = 1.333$), and compare our results with finite-difference time-domain (FDTD) numerical calculations[3] performed using the commercial software FDTD solutions from Lumerical Solutions, Inc [35]. Initially, consider that the laser beam is incident on the gold metal slab of thickness 52 nm at angles $\theta_{\mathrm{inc}} = 55.81°$

[3] The total-field scattered technique is used to reduce the needed computing resources and converging tests were performed to determine the required mesh-cell size for high accuracy results. The electric permittivity of gold is fitted to Johnson and Christy's experimental data [34] and the residual energy in the calculation volume was at least 10^{-5} of the maximum energy injected, to ensure that the continuous-wave information obtained by discrete Fourier transformations was valid.

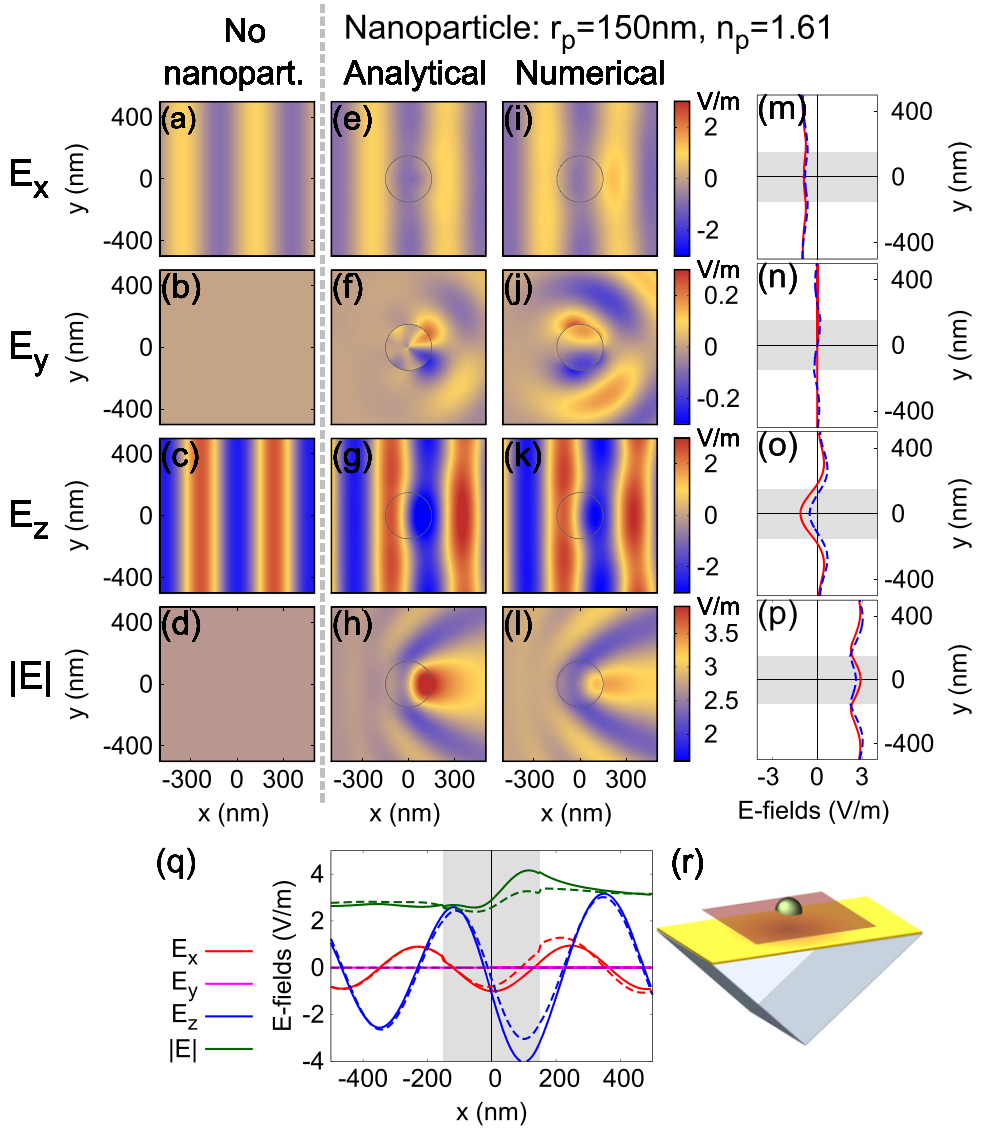

Figure 2. The *xy*-map of the diffracted surface plasmon polaritons by a single isolated nanoparticle. The nanoparticle is immersed in water $n_3 = 1.333$ with its centre at $(0,\ 0,\ -173.5$ nm), is made of polystyrene ($n_p = 1.61$) and has a radius of $r_p = 150$ nm. From top to bottom row: time snapshots of E_x, E_y and E_z, and the field map of $|E|$. (a)–(d) The E-field components when no nanoparticle is present, (e)–(h) analytical prediction and (i)–(l) numerical calculations, when the nanoparticle denoted with a black circle is present. (m)–(p) Analytical (full red line) and numerical (dashed blue line) calculations for the E-field components along the x-axis and (q) along the y-axis, passing through the centre of the nanoparticle. The shaded grey areas in (m)–(q) denote the region inside the nanoparticle. (r) An illustration of the plane for which the the E-fields are plotted.

and $\phi_{\rm inc} = 0$. Hence, the SPP-wave excited has $k_y = 0$ and (1)–(2) have only x- and z- components, which also reduces E_0 and k_{xy}. Initially, a single polystyrene nanoparticle of refractive index $n_p = 1.61$ and radius $r_p = 150$ nm is considered, positioned at $(x_0,\ y_0,\ z_0) = (0,\ 0,\ -173.5$ nm) (i.e. the nanoparticle touches the gold film at a single point), which scatters an incident SPP as described above. In figure 2, we plot the E-fields on the xy-plane parallel to the gold surface and passing through the centre of the nanoparticle (i.e. the $z = z_0$ plane), with figures 2(e)–(h) showing the analytical predictionsof (11) and figures 2(i)–(l) the FDTD numerical calculations [35], while figures 2(a)–(d) show the the E-fields when no nanoparticle is present. The E_x and E_z components do not show strong disturbances, since N is not far from unity, so the incident field $\mathbf{E}_i$ dominates over $\mathbf{E}_s$. The effect of the nanoparticle's presence is more evident from the $|E|$-field plots (figures 2(h) and (l)), where the diffracted fields induce disturbances to the constant value of $|E|$. Therefore, all features seen in figures 2(h) and (l) are due to the presence of the nanoparticle, where a shadow emerges laterally to the nanoparticle, and a bright spot immediately behind it.

Furthermore, the SPP E-field acquires a weak E_y-component, which is due to the spherical shape of the nanoparticle, that diffracts the fields in all three directions in space in a spherical manner, expressed by the Hankel function of the first kind ($h_n^{(1)}$) in the analytical work. Despite the fact that the analytical model predicts

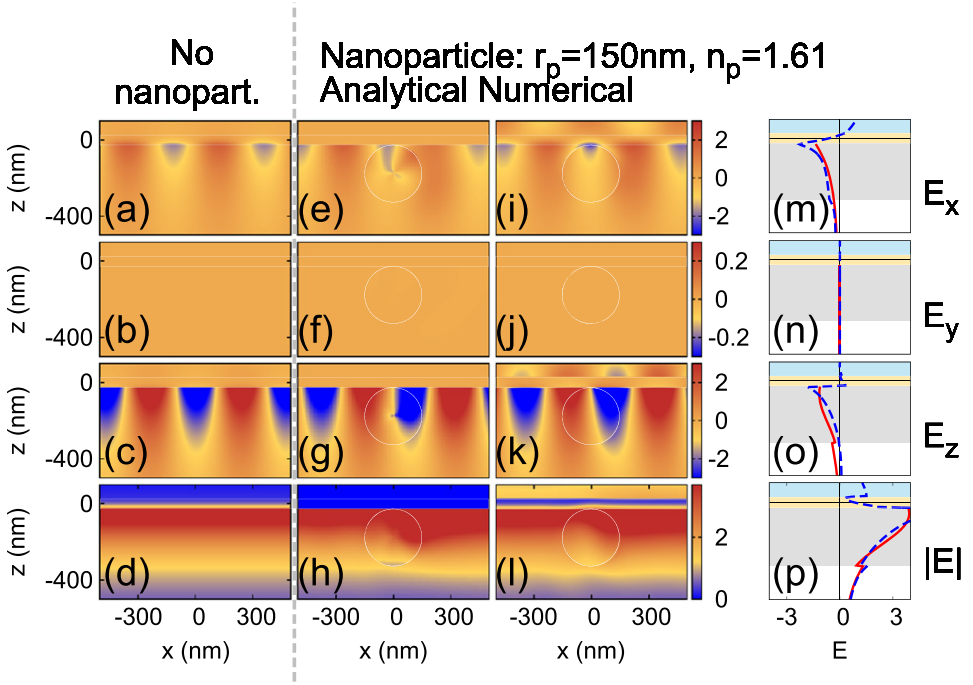

Figure 3. The *xz*-map of the diffracted surface plasmon polaritons by a single isolated nanoparticle. The nanoparticle is immersed in water $n_3 = 1.333$ with its centre at $(0,\ 0,\ -173.5\ \text{nm})$, is made of polystyrene ($n_p = 1.61$) and has a radius of $r_p = 150$ nm. From top to bottom row: time snapshots of E_x, E_y and E_z, and the field map $|E|$. (a)–(d) No nanoparticle is present. (e)–(h) Analytical predictions and (i)–(l) numerical calculations for the diffracted *E*-field components. (m)–(p) Analytical (red full line) and numerical (blue dashed line) calculations for the *E*-field along the *x*-axis, passing through the centre of the nanoparticle. The grey, yellow and blue shaded areas denote the region inside the nanoparticle, the gold film and the prim respectively.

slightly different field patterns for E_y, the amplitude is accurately predicted, leading to just minor discrepancies for $|E|$, which is the quantity determining the plasmonic-image of the nanoparticle. Also, the amplitude of E_y is one order of magnitude smaller than E_x and E_z and therefore has negligible contribution to $|E|$. In figures 2(m)–(p) and (q), we plot together for comparison analytical and numerical calculations for the *E*-field components along both the $x = x_0$ and $y = y_0$ lines of this *xy*-plane, where the shaded grey region denotes the area inside the nanoparticle. One may notice that the analytical model slightly over-estimates the $|E|$-field at the inside-back of the nanoparticle. This follows from the over-estimation of E_x and E_z-field components at the same place and comes from assuming analytically that the SPP-wave excited inside the nanoparticle has the same excitation amplitude *B* as the SPP-wave excited in water.

SPP-microscopy can image single sub-wavelength nanoparticles because SPPS are confined at the metal–water interface with massively enhanced fields, which decay exponentially away from the interface as shown in figures 3(a)–(d). In figures 3(e)–(l), we plot the analytical predictions on the *xz*-plane passing through the centre of the nanoaprticle (i.e. $y = y_0$ plane) and FDTD numerical calculations. Despite the presence of a nanoparticle, E_x and E_z field components remain highly confined at the interface of the gold–water and continue to exponentially decay away from the interface, both inside and outside the nanoparticle. The $|E|$ field map though is reduced at the front and enhanced towards the back of the nanoparticle. Then, just outside the nanoparticle $|E|$ decays along $+x$ until it reaches its original undisturbed value. In figures 3(m)–(p), the analytical and numerical calculations for the *E*-field components are plotted together for comparison along the $x = x_0$ line.

So far, we discussed the diffraction of SPP waves by a polystyrene ($n_p = 1.61$) nanoparticle of $r_p = 150$ nm, whose diameter is comparable to the SPP wavelength ($\lambda_{\text{SPP}} \sim 473$ nm). However, both the size and material composition of the particle (i.e. refractive index), affect the intensity and pattern of the diffracted SPP waves. In figure 4, we plot analytical and numerical calculations for polystyrene $n_p = 1.61$ nanoparticles of three different sizes: $2r_p = 100\ \text{nm} \sim \lambda_{\text{SPP}}/4.7$ (i.e. sub-wavelength), $2r_p = 300\ \text{nm} \sim \lambda_{\text{SPP}}/1.5$ and $2r_p = 800\ \text{nm} \sim 2\lambda_{\text{SPP}}$ (i.e. macroscopic). The $|E|$-field maps are plotted at the *xy*-plane passing through the centre of each nanoparticle. As to not overload the reader with information, we show only the $|E|$-fields maps for the various nanoparticles, normalized to the $|E|$-field when no nanoparticle is present. As expected, the larger the nanoparticle, the stronger the SPP-diffraction, which yields to a plasmonic image of higher intensity. The more prominent field patterns for larger nanoparticles can be explained by noting their larger surface area that allows

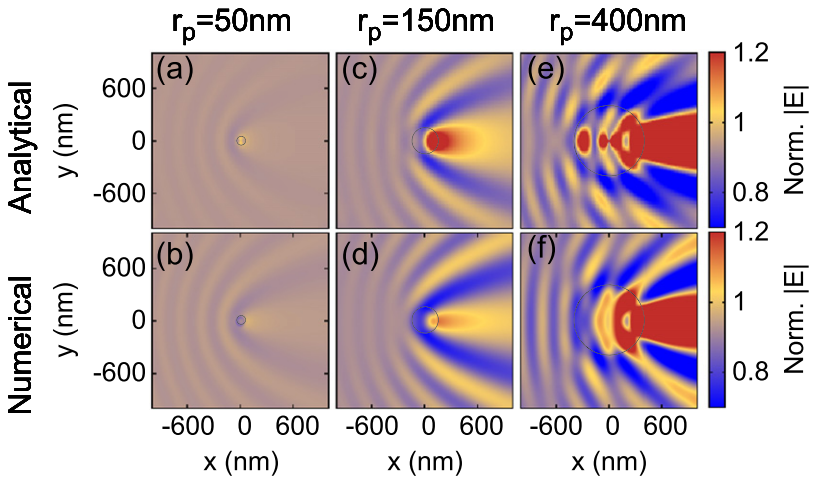

Figure 4. SPP diffraction by a polystyrene ($n_p = 1.61$) nanoparticles of various sizes. Top row are analytical predictions and bottom row numerical calculations for nanoparticle radii (a)–(b) $r_p = 50$ nm, (c)–(d) $r_p = 150$ nm and (e)–(f) $r_p = 400$ nm. The plots are normalized to the $|E|$-field when no nanoparticle is present.

for more fields to be transmitted inside the nanoparticle, which converges them (i.e. the particle mimics a lens), leading to the rear bright spots and lateral shadows.

It is impressive though to see that a sub-wavelength nanoparticle of just $r_p = 50$ nm made of polystyrene (which has a refractive index not far from the surrounding aqueous solution) causes a relatively significant diffraction to the incident SPP. Hence, a plasmonic image can be formed, recorded with the reflected beam. In fact, experiments [18, 20] have already shown that nanoparticles of dimensions $r_p = 50$ nm produce a plasmonic image. It is the nanoparticle's position within the high field enhancement of the SPP, (i.e. close to the gold–water interface) that allows for such strong field disturbances despite the fact that $\lambda_{SPP} \gg 2r_p$ and N not being far from unity. Of course, the lower signal limit for very small nanoparticles is governed by the SPP-microscope's capabilities, dominated mainly by the surface roughness of the metal slab and the sensitivity of the camera. However, it has been shown that surface roughness can be reduced to as little as $\sim\pm 1$ nm , which is indeed negligibly small from the electromagnetic point of view.

Apart from the nanoparticle's size, its material composition (i.e. its refractive index n_p) also affect the diffraction pattern and intensity. In figure 5, we show the $|E|$-field for nanoparticles immersed in water $n_3 = 1.333$ of just one radius $r_p = 150$ nm, made of three different dielectrics. We keep as a reference the polystyrene nanoparticle of $n_p = 1.61$, comparing it with nanoparticles of $n_p = 2$ and $n_p = 1$ (i.e. an air bubble in water). In fact, it is a common problem that bubbles may be unwillingly introduced in a liquid solution along with the nanoparticles, also producing plasmonic images, since their refractive index differs from water's, and therefore introducing artefacts and false readings. However, both our analytical model and numerical calculations (figures 5(a)–(b)) show that the field pattern of the diffracted wave from a bubble is complimentary to the field maps of dielectric nanoparticles (with $n_P > n_3$). Since the SPP-wave moves from a high to low dielectric medium when is transmitted inside the bubble, the rays diverge producing a shadow at its rear part and lateral bright regions. An illustration of the ray paths for nanoparticles of different n_p are shown in the top row of figure 5. For a nanoparticle of $n_p = 2$ (figures 5(e)–(f)), the diffracted fields are stronger in intensity than for the polystyrene particle, and they further converge at the rear part of the nanoparticle.

In figure 6, we plot the analytical and simulation results for the normalized $|E|$ field for all the aforementioned nanoparticle of all sizes along the x-axis. We choose to keep all nanoparticles just touching the metal surface, so the plots in figure 6(a) correspond to the fields at different z-distance from the metal interface (i.e. at $z_0 = -(r_p + d_m/2)$). In figure 6(b), one can immediately see the different field pattern for $n_p = 1$, as well as the significant field enhancement for $n_p = 2$. It is evident from this comparison figure, as well as figures 2–5 that our analytical model predicts accurately the electromagnetic interaction of a SPP with a nanoparticle of any size and material composition, with good agreement for both the amplitude and diffraction features of the E-fields.

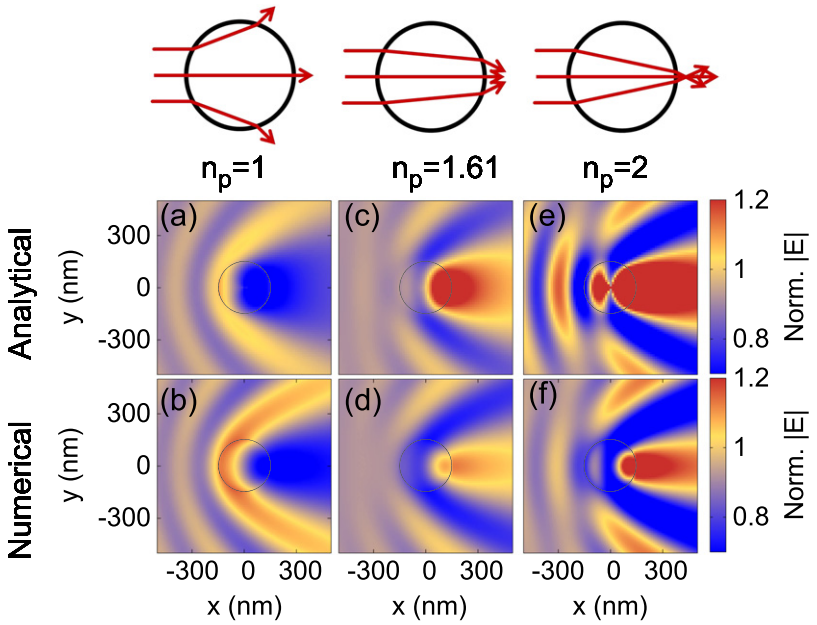

Figure 5. SPP diffraction by nanoparticles immersed in water ($n_w = 1.333$) with radius $r_p = 150$ nm made from different materials (a)–(b) $n_p = 1$ (i.e. air), (c)–(d) $n_p = 1.61$ (i.e. polystyrene) and (e)–(f) $n_p = 2$. Top figure row illustrates the different ray paths due to the relative change of n_p with respect to n_w, middle row are analytical predictions and bottom row numerical calculations for $|E|$ -fields.

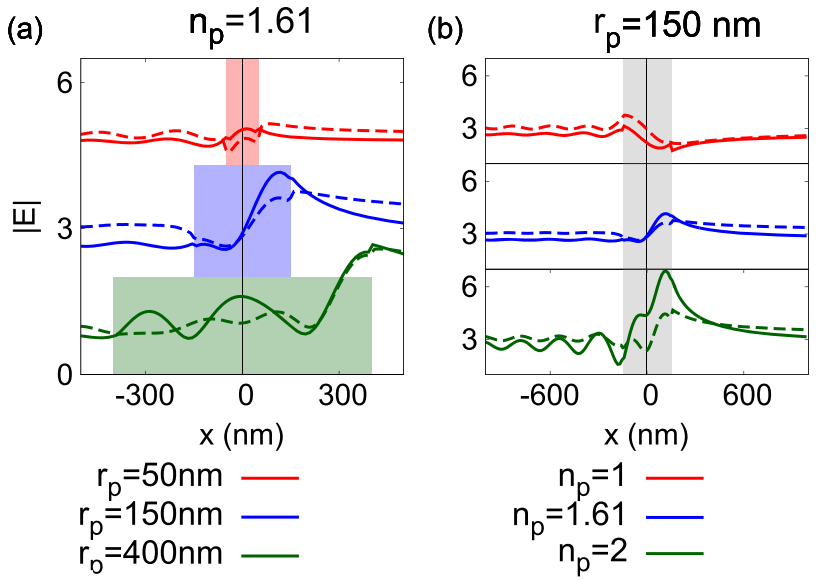

Figure 6. $|E|$-field along the x-axis passing through the centre of the particles for (a) polystyrene nanoparticles of radii $r_p = 50$ nm (red), $r_p = 150$ nm (blue), $r_p = 400$ nm (green) and (b) nanoparticles of radius $r_p = 150$ nm made of dielectrics with $n_p = 1$ (red), $n_p = 1.61$ (blue) and $n_p = 2$ (green). Shaded areas denote the regions inside the nanoparticles.

3. Plasmonic image

The plasmonic image of a nanoparticle observed with SPP-microscopy is raised from the diffraction of a SPP-wave by the nanoparticle and is always observed at exactly the reflection anlge (i.e. $-\theta_{\text{inc}}$). Hence, only the decoupling of the metal–prism SPP wave, which is carried by the right wavevector (with components $|k_{1z}|$ and k_{xy}) allows for the plasmonic image to propagate in the far-field at $-\theta_{\text{inc}}$. The metal–prism SPP-decoupling can be caused only by surface charge fluctuations in the metal, prohibiting the continuously incident laser beam to be channelled to the excited SPP-wave, and therefore creating the plasmonic image.

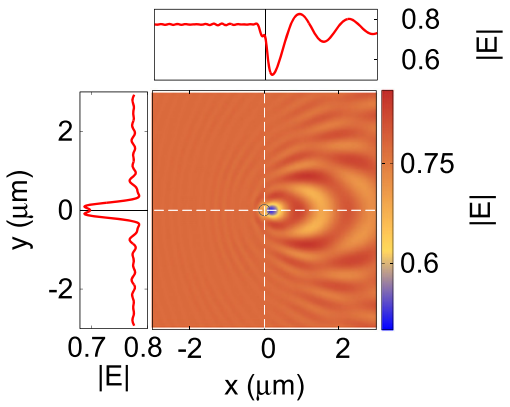

Figure 7. $|E|$-field map at the metal–prism interface. A cross-section of the nanoparticle is shown with a black circle. The $|E|$-field fluctuations are shown along the x-axis (top figure) and y-axis (left figure) passing through the centre of the nanoparticle.

The diffracted fields of the nanoparticle in the SPP-channel retain their evanescent nature and are still bound on the metal–water interface, propagating away from the nanoparticle for several wavelengths. These scattered SPP-waves then cause localized charge movements on the metal–water interface for a rather large area around the nanoparticle, which are mirrored on the metal–prism interface (in a similar but reverse way to the initial excitation of the incident SPP-wave). Also, they retain the same lateral wavevector k_{xy} as both the metal–water and metal–prism interface, with the z-component of their wavevector being k_{3z} and k_{1z} respectively. The radiative and FS-channels though, are interacting with the finite metal slab more locally, causing surface charge accumulations in the close proximity of the nanoparticle. Also, they have a different k_{xy} than the SPP waves bound on both interfaces, as well as the z-component of the wavevector varies with both θ and ϕ (i.e. across the interface). Therefore, the propagating fields emerging due to the radiative and FS-components from the nanoparticle are emitted in all θ and ϕ, and the contribution to the plasmonic image that is always recorder at $-\theta_{\text{inc}}$ is negligibly small. Hence, only the SPP-channel, for which the diffracted fields retain their SPP-nature and propagate for several wavelengths, significantly contribute to the plasmonic image.

Figure 7 shows the $|E|$-field at the metal–prism interface when a nanoparticle of $r_p = 150$ nm and $n_p = 1.61$ is present at the other side of the metal slab (the nanoparticle's position and cross-section is shown with a black circle). This $|E|$-field map contains the field disturbances caused by the SPP-, radiative- and FS-channels, as well as information for both the evanescent waves and the decoupled waves that propagate to the far-field. It should be noted that the field fluctuations are observed in a μm-scale, proving that the plasmonic image is due to the propagation and surface charge changes induces by the scattered SPP-waves (SPP-channel) from a nm-scaled particle. Figure 8 shows the $|E|$-field along the $y = 0$ and $x = 0$ axes on the metal–prism interface, where the difference to the field intensities induced by various nanoparticle is more prominent. Although the above images show how the fields change on the metal–prism interface due to the presence of various nanoparticles, the intensity patterns observed and shapes of these images do not reflect the properties of the plasmonic image, since there are contributions from the metal–prism SPP-wave and the radiative- and FS-channels that eventually produce propagating waves along all θ-angles, instead of $-\theta_{\text{inc}}$ where the plasmonic image is observed.

Since the SPP-channel is the main contributor to the plasmonic images, the decoupling wavevector is $\mathbf{k} = k_x\hat{\mathbf{e}}_x + k_y\hat{\mathbf{e}}_y + |k_{1z}|\,\hat{\mathbf{e}}_z$, which is identical to the reflected beam's wavevector. Since the z-component of the wavevector is not imaginary any more, then the plasmonic image is always detected at $-\theta_{\text{inc}}$. It follows then, that the plasmonic image of a nanoparticle of radius r_p and refractive index n_p is given by:

$$\mathbf{E}_{\text{image}} = \frac{A\,\exp\left(-|k_{1z}|\,d_m/2 - \mathrm{i}\,|k_{1z}|\,z\right)}{\omega\varepsilon_0\varepsilon_1|n_p|\sqrt{I_i}} \sum_{n=0}^{\infty}\sum_{m=-n}^{m=n} 4\pi\mathrm{i}^n\left(a_{n\theta}E_{0\theta}\hat{\mathbf{e}}_\theta + a_{n\phi}E_{0\phi}\hat{\mathbf{e}}_\phi\right) \times h_n^{(1)}\left(k_{xy}r\right)Y_n^m(\theta,\phi)\,\overline{Y_n^m\left(\theta_{k_1},\phi_{k_1}\right)}, \tag{12}$$

where $\exp\left(k_{1z}d_m/2\right)$ defines the amplitude of the decoupled wave that propagates to the far-field, $a_{n\theta}, a_{n\phi}, E_{0\theta}$ and $E_{0\phi}$ define the shape of the plasmonic image and I_i is the intensity of the SPP wave incident on the nanoparticle, which depends on the radius of the nanoparticle n_p and its distance d_{sep} from the metal slab and is given by:

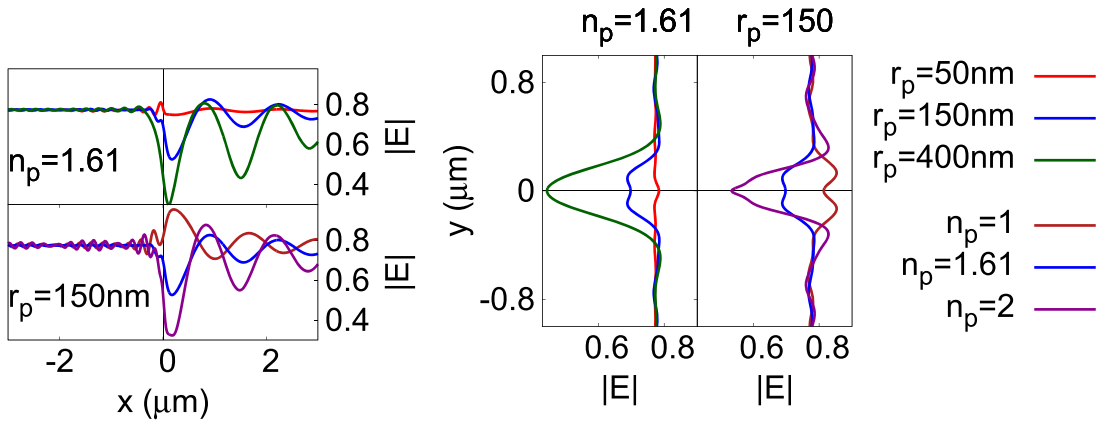

Figure 8. $|E|$-field fluctuations along the x-axis (left figure) and y-axis (right figure) passing through the centre of the nanoparticle, for polystyrene ($n_p = 1.61$) nanoparticles of $r_p = 50$ nm (red line), $r_p = 150$ nm (blue line) and $r_p = 400$ nm (green line), and nanoparticle of $r_p = 150$ nm made of $n_p = 1$ (brown line), $n_p = 1.61$ (blue line) and $n_p = 2$ (purple line).

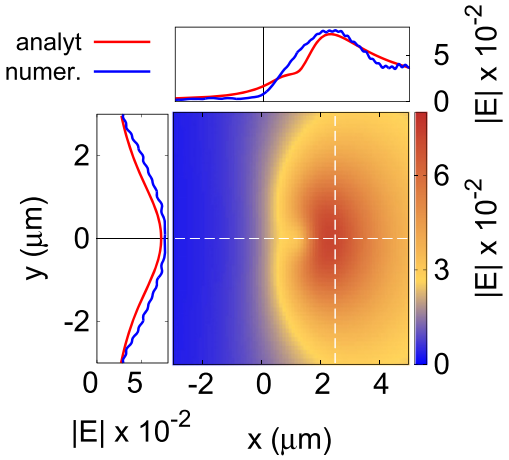

Figure 9. Plasmonic image (i.e. $|E|$-field) at $z = 950$ nm from the metal–prism interface. The plasmonic image is plotted along the x-axis (top figure) and parallel to the y-axis at $x = 2.460$ μm (left figure), indicated with white dash lines, for both the analytical prediction (red line) and numerical calculations (blue line).

$$I_i = |B|^2 \varepsilon_3^2 \pi \, \sinh\left(2\left|k_{3z}\right| r_p\right) \exp\left(\left|k_{3z}\right| d_{\text{sep}}\right) \Big/ \left(\left|k_{3z}\right| r_p\right). \tag{13}$$

We plot in figure 9 the above equation which describes the plasmonic image along with numerical calculations at a distance $z \sim 950$ nm from the metal–prism interface for a polysteryne ($n_p = 1.61$) nanoparticle of $r_p = 150$ nm. We choose such a large distance from the interface, to ensure that the SPP-fields from the metal–prism interface have decayed. Hence the simulation results (which cannot distinguish between evanescent or propagating fields) do not include the evanescent component. We also subtract from the numerical results the background contribution from the reflection from the slab, such that the recorded fields from the simulation calculation would be zero at $z \sim 950$ nm when no nanoparticle is present in medium 3. Both the analytical prediction of (12) and numerical calculations show a 'bean'-shaped image with almost identical intensities. It should be noted that the plasmonic image shown in figure 9 is still located in the prism and has not been transferred to the far-field, where images are experimentally recorded with SPP-microscopy.

Figure 10 shows analytical and numerical results for the plasmonic images of nanoparticles of various sizes (sub-wavelength to macroscopic) and made of various dielectric materials. As the size of the nanoparticle increases, the intensity of the plasmonic image increases, while its geometrical features remain the same. This is in agreement with experimental observations [17], where the plasmonic image obtained for nanoparticles (even of $r_p \sim \lambda_{\text{SPP}}$) is a bright spot whose intensity is dependent on the size of the particle. Also, for nanoparticles of the same size ($r_p = 150$ nm), the intensity of the plasmonic image changes as the refractive index of the nanoparticles deviates from its environment's (i.e. $|n_p - n_3|$). Hence, for nanoparticles in an aqueous solution ($n_3 = 1.333$), the intensity (bright spot) of the image observed by a bubble ($n_p = 1$) and a polystyrene

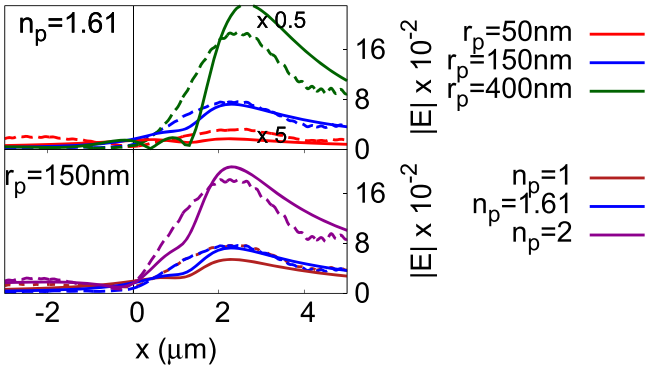

Figure 10. The plasmonic images (i.e. $|E|$-fields) at $z = 950$ nm away from the metal–prism interface for various nanoparticles. The analytical predictions (full lines) and numerical calculations (dashed lines) for the plasmonic images of polystyrene ($n_P = 1.61$) nanoparticles (top figure) of $r_p = 50$ nm (red line), $r_p = 150$ nm (blue line) and $r_p = 400$ nm (green line) and for nanoparticles with $r_p = 150$ nm (bottom figure) with refractive index of $n_p = 1$ (brown line), $n_p = 1.61$ (blue line) and $n_p = 2$ (purple line).

nanoparticle ($n_p = 1.61$) are of similar intensities, but of different tail intensities (i.e. at the $-x$-axis). Finally, the analytical model proposed here predicts very accurately both the geometrical features and the intensity of the plasmonic image. With our analytical model, one can obtain any of the above results in just few tens of a second using a standard computer, while the FDTD simulations require ~48 hours run on a significantly more powerful computing system. Hence, it is a valuable and fast tool towards the spectroscopic characterization of isolated nanoparticles from sub-wavelength to macroscopic dimensions, through SPP-microscopy techniques.

4. Conclusions

In the present study we present a full-wave analytical theory that describes the principles governing the formation of plasmonic images with SPP-microscopy techniques. We show the diffraction field maps from both our analytical model and numerical calculations, which highlight the physics of the diffraction process. Then, through our analytical model, we show that only the SPP-to-SPP scattering channel contributes to the plasmonic image. The dependence of the plasmonic image's properties on the particle's size and material composition are studied from sub-wavelength to macroscopic nanoparticles, and are in agreement with experimental observations. Hence, our analytical model allows for an insight to the spectroscopic characterization of a single isolated nanoparticle of even sub-wavelength dimensions, invigorating the capabilities of SPP-microscopy techniques.

Acknowledgments

The research leading to these results has received funding from the European Union Seventh Framework Programme (FP7/2007-2013) under grant agreement no 280478. The work was stimulated by discussion with Prof Vladimir Mirsky and Dr Alexander Zybin, and the experimental findings of their groups.

Appendix. SPP-wave equation in spherical harmonics

The incident SPP E-field on a nanoparticles shown in equation (1) in Cartesian coordinates can be written as:

$$\mathrm{E}_i = \frac{B\,\exp\left(\left|k_{3z}\right|z\right)}{\omega\varepsilon_3\varepsilon_0}\mathrm{E}_0\,\exp\left(\mathrm{i}k_x x + \mathrm{i}k_y y\right), \tag{A.1}$$

where

$$B = A\frac{\mathrm{e}^{\left(\left|k_{3z}\right|-\left|k_{1z}\right|\right)\frac{d_m}{2}}}{2\left|k_{2z}\right|/n_2^2}\left[\mathrm{e}^{-\left|k_{2z}\right|d_m}\left(\frac{\left|k_{2z}\right|}{n_2^2}-\frac{\left|k_{1z}\right|}{n_1^2}\right)+\mathrm{e}^{\left|k_{2z}\right|d_m}\left(\frac{\left|k_{1z}\right|}{n_1^2}+\frac{\left|k_{2z}\right|}{n_2^2}\right)\right] \tag{A.2}$$

and A coefficient is related to the incident intensity of the fields and for our system $A \sim \sqrt{\frac{\varepsilon_0}{\mu_0}}\frac{\varepsilon_3}{\varepsilon_1}E_0$, and E_0 is the electric field amplitude in vacuum of the incident field on the metal slab. By separating its evanescent, vector and

phase propagating components, it can be expressed in spherical harmonics. The evanescent decay of the SPP is governed by: $\exp\left(|k_{3z}|\,z\right)$ term. Since this term is non-radiative: $\exp\left(|k_{3z}|\,z\right) = \exp\left(|k_{3z}|\,r\,\cos\theta\right)$. The vector direction of $\mathbf{E}_i$ is determined by $\mathbf{E_0}$ is transformed in spherical coordinates using:

$$\begin{bmatrix}\hat{\mathbf{e}}_x\\ \hat{\mathbf{e}}_y\\ \hat{\mathbf{e}}_z\end{bmatrix} = \begin{bmatrix}\sin\theta\cos\phi & \cos\theta\cos\phi & -\sin\phi\\ \sin\theta\sin\phi & \cos\theta\sin\phi & \cos\phi\\ \cos\theta & -\sin\theta & 0\end{bmatrix}\begin{bmatrix}\hat{\mathbf{e}}_r\\ \hat{\mathbf{e}}_\theta\\ \hat{\mathbf{e}}_\phi\end{bmatrix}. \tag{A.3}$$

Therefore, $\mathbf{E_0}$ becomes:

$$\mathbf{E}_0 = -\mathrm{i}\left|k_{3z}\right|\hat{\mathbf{e}}_x - \mathrm{i}\left(\frac{\left|k_{3z}\right|k_y}{k_x}\right)\hat{\mathbf{e}}_y - \left(k_x + \frac{k_y^2}{k_x}\right)\hat{\mathbf{e}}_z = E_{0i}^r\hat{\mathbf{e}}_r + E_{0i}^\theta\hat{\mathbf{e}}_\theta + E_{0i}^\phi\hat{\mathbf{e}}_\phi, \tag{A.4}$$

where

$$\begin{aligned}E_{0i}^r &= -\mathrm{i}\left|k_{3z}\right|\sin\theta\cos\phi - \mathrm{i}\frac{k_y\left|k_{3z}\right|}{k_x}\sin\theta\sin\phi + \left(k_x + \frac{k_y^2}{k_x}\right)\cos\theta,\\ E_{0i}^\theta &= -\mathrm{i}\left|k_{3z}\right|\cos\theta\cos\phi - \mathrm{i}\frac{k_y\left|k_{3z}\right|}{k_x}\cos\theta\sin\phi - \left(k_x + \frac{k_y^2}{k_x}\right)\sin\theta,\\ E_{0i}^\phi &= \mathrm{i}\left|k_{3z}\right|\sin\phi - \mathrm{i}\frac{k_y\left|k_{3z}\right|}{k_x}\cos\phi.\end{aligned} \tag{A.5}$$

Finally the propagating component of equation (1), which drives the phase propagation of the SPP wave is given by: $\exp\left(\mathrm{i}k_x x + \mathrm{i}k_y y\right)$, and can be expressed in spherical harmonics by using the Jacobi–Angler expansion as:

$$\exp\left(\mathrm{i}k_x x + \mathrm{i}k_y y\right) = \sum_{n=0}^{\infty}\sum_{m=-n}^{m=n} 4\pi\mathrm{i}^n j_n\left(k_{xy}r\right)Y_n^m(\theta,\phi)\,\overline{Y_n^m\left(\theta_k,\phi_k\right)}, \tag{A.6}$$

where j_n is the spherical Bessel function, $k_{xy} = \sqrt{k_x^2 + k_y^2}$ is the propagating wavevector of the SPP, r, θ and ϕ are the spatial spherical coordinates with origin at a point (x_0, y_0, z_0). θ_k and ϕ_k are the spherical components of $\mathbf{k}_{xy}$ wavevector, and since no k_z component exists in the propagating term $\exp\left(\mathrm{i}k_x x + \mathrm{i}k_y y\right)$, then one can take that $\theta_k = \pi/2$. Y_n^m is the spherical harmonic function, which is given by: $Y_n^m(\theta,\phi) = \sqrt{\frac{(2n+1)(n-m)!}{4\pi(n+m)!}}P_n^m(\cos\theta)\mathrm{e}^{\mathrm{i}m\phi}$, where P_n^m is the associated Legendre Polynomial and $\overline{Y_n^m}$ is its complex conjugate. Hence, the E-field of a SPP wave in spherical harmonics is given by:

$$\mathbf{E}_i = \frac{B\exp\left(\left|k_{3z}\right|r\,\cos\theta\right)}{\omega\varepsilon_3\varepsilon_0}\mathbf{E}_0\sum_{n=0}^{\infty}\sum_{m=-n}^{m=n} 4\pi\mathrm{i}^n j_n\left(k_{xy}r\right)Y_n^m(\theta,\phi)\,\overline{Y_n^m\left(\theta_k,\phi_k\right)}. \tag{A.7}$$

References

[1] Myszka D G 1999 Improving biosensor analysis *J. Mol. Recognit.* **12** 279–84
[2] Navratilova I, Sodroski J and Myszka D G 2005 Solubilization, stabilization, and purification of chemokine receptors using biosensor technology *Anal. Biochem.* **339** 271–81
[3] Shuman C F, Hamalainen M D and Helena Danielson U 2004 Kinetic and thermodynamic characterization of HIV-1 protease inhibitors *J. Mol. Recognit.* **17** 106–19
[4] Morton T A and Myszka D G 1998 Kinetic analysis of macromolecular interactions using surface plasmon resonance biosensors *Methods Enzymology* **295** 268–82
[5] Weiss M N, Srivastava R and Groger H 1996 Experimental investigation of a surface plasm-based integrated-optic humidity sensor *Electron. Lett.* **32** 842–3
[6] Chadwick B and Gal M 1993 An optical temperature sensor using surface plasmons *Japan. J. Appl. Phys.* **32** 2716
[7] Jung C C, Saban S B, Yee S S and Darling R B 1996 Chemical electrode surface plasmon resonance sensor *Sensors Actuators* B **32** 143–7
[8] van Gent J, Lambeck P V, Bakker R J, Popma T J, Sudholter E J R and Reinhoudt D N 1991 Design and realization of a surface plasmon resonance-based chemo-optical sensor *Sensors Actuators* A **26** 449–52
[9] Miwa S and Arakawa T 1996 Selective gas detection by means of surface plasmon resonance sensors *Thin Solid Films* **281-282** 466–8
[10] Abdelghani A, Chovelon J M, Jaffrezic-Renault N, Ronot-Trioli C, Veillas C and Gagnaire H 1997 Surface plasmon resonance fiber-optic sensor for gas detection *Sensors and Actuators* B **38-39** 407–10
[11] Sota H, Hasegawa Y and Iwakura M 1998 Detection of conformational changes in an immobilized protein using surface plasmon resonance *Anal. Chem.* **70** 2019–24

[12] Ohlson S, Jungar C, Strandh M and Mandenius C-F 2000 Continuous weak-affinity immunosensing *Trends Biotechnol.* **18** 49–52
[13] Oh B-K, Kim Y-K, Lee W, Bae Y M, Hong Lee W and Choi J-W 2003 Immunosensor for detection of Legionella pneumophila using surface plasmon resonance *Biosens. Bioelectron.* **18** 605–11
[14] Minunni M and Mascini M 1993 Detection of pesticide in drinking water using real-time biospecific interaction analysis (bia) *Anal. Lett.* **26** 1441–60
[15] Homola J, Dostalek J, Chen S, Rasooly A, Jiang S and Yee S S 2002 Spectral surface plasmon resonance biosensor for detection of staphylococcal enterotoxin B in milk *Int. J. Food Microbiology* **75** 61–69
[16] Nayeri F, Aili D, Nayeri T, Xu J, Almer S, Lundstrom I, Akerlind B and Liedberg B 2005 Hepatocyte growth factor (HGF) in fecal samples: rapid detection by surface plasmon resonance *BMC Gastroenterology* **5** 13
[17] Zybin A, Kuritsyn Y A, Gurevich E L, Temchura V V, Uberla K and Niemax K 2010 Real-time detection of single immobilized nanoparticles by surface plasmon resonance imaging *Plasmonics* **5** 31–35
[18] Yu H, Shan X, Wang S, Chen H and Tao N 2014 Plasmonic imaging and detection of single DNA molecules *ACS Nano* **18** 3427–33
[19] Halpern A R, Wood J B, Wang Y and Corn R M 2014 Single-nanoparticle near-infrared surface plasmon resonance microscopy for real-time measurements of DNA hybridization adsorption *ACS Nano* **8** 1022–30
[20] Wang S, Shan X, Patel U, Huang X, Lu J, Li J and Tao N 2010 Label-free imaging, detection, and mass measurement of single viruses by surface plasmon resonance *Proc. Natl Acad. Sci. USA* **107** 16028–32
[21] Prieve D C and Walz J Y 1993 Scattering of an evanescent surface wave by a microscopic dielectric sphere *Appl. Opt.* **32** 1629–41
[22] Evlyukhin A B, Brucoli D G, Martīn-Moreno L, Bozhevolnyi S I and Garcīa-Vidal F J 2007 Surface plasmon polariton scattering by finite-size nanoparticles *Phys. Rev.* B **76** 075426
[23] Kornyshev A A, Marinescu M, Paget J and Urbakh M 2012 Reflection of light by metal nanoparticles at electrodes *Phys. Chem. Chem. Phys.* **14** 1850–9
[24] Bozhevolnyi S I and Coello V 1998 Elastic scattering of surface plasmon polaritons: modelling and experiment *Phys. Rev.* B **58** 10899–910
[25] Baumeier B, Huerkamp F, Leskova T A and Maradudin A A 2011 Scattering of surface-plasmon polaritons by a localized dielectric surface defect studied using an effective boundary condition *Phys. Rev.* A **84** 013810
[26] Shchegrov A V, Novikov I V and Maradudin A A 1997 Scattering of surface plasmon polaritons by a circularly symmetric surface defect *Phys. Rev. Lett.* **78** 4269
[27] Shchegrov A V, Novikov I V and Maradudin A A 1997 Scattering of surface plasmon polaritons by a circularly symmetric surface defect *Phys. Rev. Lett.* **79** 2597
[28] Arias R E and Maradudin A A 1997 Scattering of a surface plasmon polariton by a localized dielectric surface defect *Opt. Express* **21** 9734
[29] Navarro-Cia M, Natrella M, Dominec F, Delagnes J C, Kuzel P, Mounaix P, Graham C, Renaud C C, Seeds A J and Mitrofanov O 2013 Terahertz imaging of sub-wavelength particles with Zenneck surface waves *Appl. Phys. Lett.* **103** 221103
[30] Maier S A 2007 *Plasmonics: Fundamentals and Applications* (Berlin: Springer)
[31] Sanchez-Gil J A and Maradudin A A 1999 Near-field and far-field scattering of surface plasmon polaritons by one-dimensional surface defects *Phys. Rev.* B **60** 8359–67
[32] Sanchez-Gil J A 1998 Surface defect scattering of surface plasmon polaritons: mirrors and light emitters *Appl. Phys. Lett.* **73** 3509–11
[33] Zayats A V, Smolyaninov I I and Maradudin A A 2005 Nano-optics of surface plasmon polaritons *Phys. Rep.* **408** 131–314
[34] Johnson P B and Christy R W 1972 *Phys. Rev.* B **6** 4370
[35] Lumerical Solutions Inc. http://lumerical.com